



LAWRENCE
LIVERMORE
NATIONAL
LABORATORY

Micro-shaping, polishing and damage repair of glass surfaces using focused infrared laser beams

M. J. Matthews, S. T. Yang, S. Elhadj, N. Shen, R. N. Raman, G. M. Guss, I. L. Bass, M. C. Nostrand, P. J. Wegner

May 8, 2014

Advanced Engineering Materials

Disclaimer

This document was prepared as an account of work sponsored by an agency of the United States government. Neither the United States government nor Lawrence Livermore National Security, LLC, nor any of their employees makes any warranty, expressed or implied, or assumes any legal liability or responsibility for the accuracy, completeness, or usefulness of any information, apparatus, product, or process disclosed, or represents that its use would not infringe privately owned rights. Reference herein to any specific commercial product, process, or service by trade name, trademark, manufacturer, or otherwise does not necessarily constitute or imply its endorsement, recommendation, or favoring by the United States government or Lawrence Livermore National Security, LLC. The views and opinions of authors expressed herein do not necessarily state or reflect those of the United States government or Lawrence Livermore National Security, LLC, and shall not be used for advertising or product endorsement purposes.

Micro-shaping, polishing and damage repair of glass surfaces using focused infrared laser beams**

By Manyalibo J. Matthews, * Steven T. Yang, Nan Shen, Selim Elhadj, Rajesh N. Raman, Gabe Guss, Isaac L. Bass, Michael C. Nostrand and Paul J. Wegner

[*] Dr. M. J. Matthews, Dr. S. T. Yang, Dr. N. Shen, Dr. S. Elhadj, Dr. R. N. Raman, Mr. G. Guss, Dr. I. L. Bass, Dr. M. C. Nostrand and Dr. P. J. Wegner
Lawrence Livermore National Laboratory
Livermore CA 94550, U.S.A.

[**] This work was supported by LLNL Lab-Directed Research and Development (LDRD) grants 08-ERD-057 and 11-ERD-026. This work was performed under the auspices of the U.S. Department of Energy by Lawrence Livermore National Laboratory under Contract DE-AC52-07NA27344. Laboratory assistance from N. Nielsen, B. Woods and D. Cooke is gratefully acknowledged.

Abstract

Localized infrared (IR) laser heating of fused silica optics has proven highly effective in reducing or removing surface flaws which tend to limit performance in high power laser systems. Here we present both simulation and experimental results to examine the use of IR laser light to polish, anneal and micro-shape fused silica surfaces used in high power laser systems. We show how the resulting material response can be tuned by considering the temperature-dependent optical constants of the material and choosing the appropriate laser parameter set. For example, non-evaporative laser polishing of glass surfaces to heal crack networks is shown most effective when using mid-IR lasers which lead to laser energy coupling up to ~ 1 mm in depth. In contrast, long-wave IR light tuned to the Reststrahlen frequency of the material is shown to evaporate material most efficiently with penetration depths of < 1 μm . Through calibrated, time-resolved thermal imaging we are able to monitor the laser polishing process, to control material response. The results of our studies can be applied beyond the practical application of damage mitigation in high energy pulsed laser systems to any which require laser-smoothing and shaping of glass surfaces.

1. Introduction

Thermomechanical modification of nano- and micro-structures on a wide variety of material surfaces to create or enhance surface properties using long-wave CO₂ lasers has enjoyed significant success in recent decades.^[1] Recently, localized CO₂ laser heating of silica glass has been successfully applied to control and mitigate surface damage on optics used in high power laser applications such as inertial confinement fusion (ICF).^[2] Because the nano- and micro-scale fractured surfaces associated with polishing/machining are believed to be associated with a higher concentration of UV-absorbing damage precursors, thermal treatment can act to allow these defects to anneal by way of surface or bulk diffusion. Additionally, enhancement of local field intensity from irregular interfaces, clearly present on optically damaged and laser machined surfaces, could also act to lower the damage threshold of laser optics.^[3] In this case, CO₂ laser heating can act to macroscopically smooth or ‘fire polish’ these surfaces into more regular interfaces, thus lowering near-field intensification effects. However, despite the long history of IR laser processing of silica optics, few attempts have been made to understand the energy coupling and heat flow in order to optimize material processing.

The present work details efforts to understand the energy deposition of infrared laser light into fused silica surfaces for the purpose of polishing and repairing surface flaws to produce surface finishes suitable for high power laser systems. We first describe the mid- and far-IR laser systems used to process fused silica surfaces and the *in situ* thermal imaging used to measure laser-induced temperature changes. We show that, depending on the polish and surface figure requirements, the IR laser parameters (wavelength, pulse length, power, beam size) can be adjusted to optimize the thermal and mechanical response of the material. Predicted temperatures and heat affected zones based on finite element modeling are found to compare well with experiment. Finally we demonstrate the use of IR lasers to mitigate

damaged fused silica surfaces and the effect of various laser treatments on surface morphology, residual stress and laser-induced damage threshold.

2. Experimental section

2.1 Materials

The fused silica parts used in this study were UV-grade Type III (800-1000ppm wt.% OH) glass 7980 from Corning (NY, USA). All samples are 51 mm in diameter and 10 mm thick prepared with an optical polish and light HF etch to remove impurities. All experiments were conducted in ambient air.

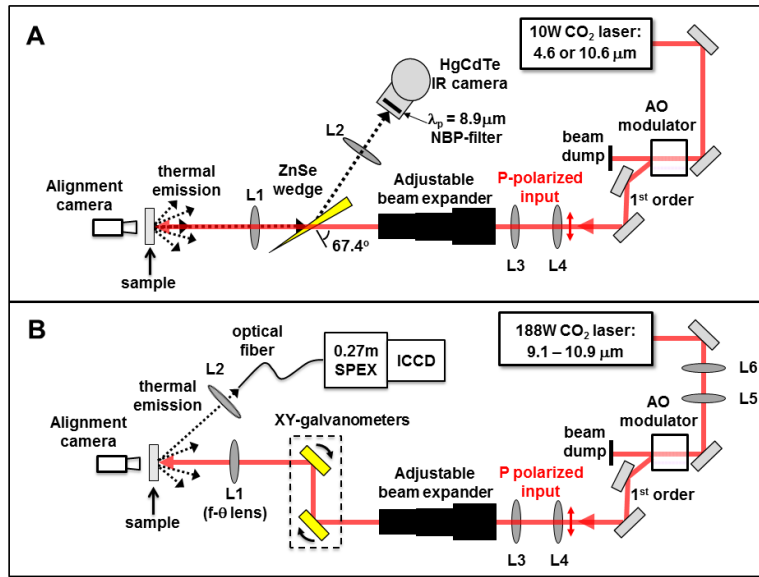


Figure 1: Schematic of optical system and MCT camera used for in-situ surface temperature measurement of CO₂ laser heated samples. The red solid line marks the CO₂ laser beam path; the blue dotted line indicates the emitted thermal emission. L1-L6 are ZnSe lenses; an adjustable beam expander is used to vary final beam size; NBP is the narrow-band bandpass cold filter centered at 8.9 μm placed immediately in front of the MCT camera; ICCD is an intensified-gated CCD camera.

2.2 Laser-based thermal processing and temperature measurement

Figure 1 above displays the two laser processing setups used in the present study. In both setups laser light is modulated temporally using an acousto-optic modulator (AOM) and transported using high reflectors, a beam expander and ZnSe lenses to the sample surface. A

motorized stage and inspection microscope are common to both systems as well. In Fig. 1A a ~ 10 W 4.6 μm or 10.6 μm laser is used in an annealing mode where laser light illuminates ~ 1 mm of sample surface over 10's of seconds exposure time τ while the sample is scanned with a motorized stage. Thus, typical irradiances in this setup are $< 1 \text{ kW/cm}^2$. The setup of Fig. 1A is equipped with a calibrated HgCdTe camera with a narrow 8.9 μm band pass filter to measure transient surface temperature as described previously.^[4, 5] The thermal emission from the sample is coupled to the HgCdTe camera through a ZnSe wedge which is oriented at Brewster's angle (67.4°). In contrast, the micro-patterning setup in Fig. 2B processes samples at much higher irradiances ($\sim 1 \text{ MW/cm}^2$) by tightly focusing 9~11 μm tunable laser light into 100-500 μm diameters over 10's of microseconds. The laser beam is rastered across the sample using a pair of scanning galvanometer mirrors positioned just prior to the final f- θ scanning lens (L1). By synchronizing the AOM and galvanometers, precise micro-machining of fused silica surfaces can be used to machine away defects and repair damaged optics. To measure peak temperatures, the setup in Fig. 1A is equipped with a gated intensified CCD (ICCD) camera and spectrometer (SPEX 270) to resolve the thermal emission spectrum.

2.3 Microscopic surface characterization: Raman and Atomic Force Microscopies

The surface morphology of laser polished regions was characterized before and after exposure using a Digital Instrument Dimension 3100 atomic force microscope (AFM). Instrument resolution was < 1 nm vertically and ~ 10 nm laterally. Spatially-resolved variations in Si-O bonding structure caused by laser heating was measured using confocal Raman microscopy operating at 532 nm (CW), with a lateral, depth and spectral resolution of 1 μm , 5 μm and 4 cm^{-1} respectively.^[6] Changes in molecular structure in the silica glass were

quantified by extracting a fictive temperature (T_f) from the measured TO-mode frequency shift at $\nu_{\text{TO}} \sim 1060 \text{ cm}^{-1}$ using well-known scaling laws.^[7]

3. Finite element modelling of laser-heated glass

A 2D axisymmetric geometry is used to describe the volumetric energy deposited into a 10x50 mm silica domain as a function of time t , radial position from the center of the beam r , and depth into the sample z :

$$Q(r, z, t, T) = \frac{P(t)\beta(T)}{\pi a^2} \exp(-\beta(T)z) \exp\left[-\left(\frac{r}{a}\right)^2\right] \quad (1)$$

In Eq. (3), $P(t)$ is the deposited time-dependent laser power (reduced by Fresnel reflection at the surface), $\beta(T)$ is the temperature-dependent laser absorption coefficient^[8, 9] and a is the 1/e radius of the Gaussian beam. $\beta(T=300 \text{ K})$ ranges from $\sim 1 \text{ mm}$ at $\lambda_L=4.6 \text{ }\mu\text{m}$, to $\sim 300 \text{ nm}$ at $\lambda_L=9.2 \text{ }\mu\text{m}$. At $\lambda_L=10.6 \text{ }\mu\text{m}$, $\beta(T=300 \text{ K}) \sim 40 \text{ }\mu\text{m}$. A highly non-uniform finite-element mesh of $\sim 8,000$ elements is used in the simulations. The element size ranged from $1 \text{ }\mu\text{m}$ directly below the laser to $500 \text{ }\mu\text{m}$ at the opposite boundary of the sample. The nonlinear heat equation is given as

$$\rho(T)C_p(T)\frac{\partial T}{\partial t} - \nabla(\kappa(T) \cdot \nabla T) = Q(r, z, t, T) \quad (2)$$

where ρ , C_p and κ are the mass density, heat capacity at constant pressure and thermal conductivity, respectively. Material properties were taken from vendor data or extrapolated using kinetic theory as described in detail elsewhere.^[10] Heat transfer boundary conditions for laser-heating problems typically include surface convection, radiation, and evaporative cooling but are highly dependent on the temperature range of interest. For $T > 2000 \text{ K}$, an evaporative heat loss term^[11] is applied to the incident surface. However, radiative and convective loss from the surface can be shown to be negligible.^[10]

A standard relaxation model is used in conjunction with the calculated thermal histories to extract relaxation parameters from spatially-resolved Raman data.^[6] Because the fictive temperature is a measure of the structural deviation of the glass from the original annealed state, changes in T_f are used below to assess the spatial distribution of the laser heat affected zone. Furthermore, because T_f can be assessed beneath the laser heated surface, they complement the direct surface thermodynamic temperature measurements and allow a better view of the 3 dimensional temperature histories.

4. Results and Discussion

4.1 Laser-induced temperature distribution and power scaling

Figure 2A shows the measured peak surface temperature at beam center, just before turn off of the 10 s long laser pulse, plotted as a function of incident laser power (P) normalized to beam size (a) for 1/e beam diameters of $\sim 250 \mu\text{m}$ and

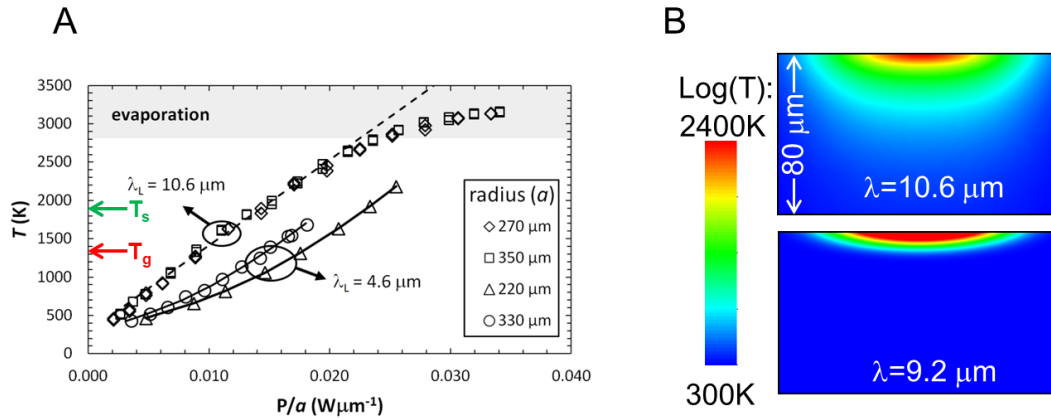


Figure 2: (A) Experimental (symbols) and calculated (lines) on-axis surface temperature derived from IR-imaging for fused silica heated using a $10.6 \mu\text{m}$ and a $4.6 \mu\text{m}$ CO_2 laser as indicated by the circles with arrows ($t_{\text{exp}} = 5 \text{ sec}$). The data is for the beam radii, a , plotted over the normalized axis using the laser power, P , and the 1/e radii. The evaporation regime is delineated by the grayed area while the glass transition and softening temperatures are indicated by T_g and T_s respectively. (B) Transient temperature profiles near the Restrahl frequency in silica for $P = 34 \text{ W}$, $\tau = 12.5 \mu\text{s}$ and $d = 130 \mu\text{m}$.

~340 μm and for mid- and far-IR laser systems. For $\lambda_L=4.6$ μm , the peak surface temperature is seen to rise up in a nonlinear fashion as the P/a is increased. This is in sharp contrast with the 10.6 μm laser heating case, where the temperature rise is found to be linear up to ~2800 K.^[4] Above 2800 K, the peak temperature approaches a limiting value of 3100 K, independent of beam radius due to evaporative cooling.^[11] The nonlinear temperature rise in the 4.6 μm case is a result of the temperature dependence of the absorption coefficient^[8] and the fact that the absorption depth is comparable to the laser beam size.^[12] Thus, as temperature increases, fused silica absorption length shortens which in turn leads to more heat deposition close to the surface and, therefore, to an accelerated rise in surface temperature. Moreover, the nonlinear temperature rise versus power implies that the heating of fused silica using a 4.6 μm laser is relatively more sensitive to potential power fluctuations.^[13] Hence, a more stringent power control would be required for the 4.6 μm laser over that of the 10.6 μm laser to obtain consistent laser annealing results. Interestingly, for the 10.6 μm case, the change in beam radius had a negligible effect on the nature of the surface absorption since the absorption depth is already very shallow relative to the beam size.

Although 10.6 μm CO₂ lasers are by far the most common in industry due to gain efficiency, optimal energy coupling need not occur at this wavelength. Indeed, a minimum in absorption depth for fused silica at room temperature is found near ~9.2 μm ,^[14] implying laser processing at this wavelength would yield very confined heating zones and linear temperature rise with laser power. However, due to thermal diffusion, the tightly confined heating region is only realized for times $<\tau_{th}\sim 30$ ms for a 500 μm beam size. Figure 2B shows a comparison of the calculated temperature profile for a 12.5 μs pulsed laser exposure at the peak absorption wavelength $\lambda_L=9.2$ μm and at the more widely used wavelength $\lambda_L=10.6$ μm . As

will be shown later, use of $\sim 9.2 \mu\text{m}$ wavelengths can be exploited to limit the heat affected zone when applying evaporative, micro-shaping techniques for damage mitigation.

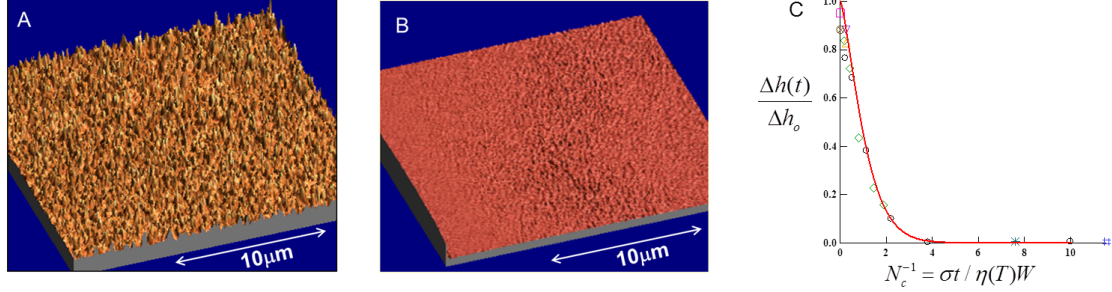


Figure 3: AFM profiles of roughened silica surfaces before (A) and after (B) laser heating with a $10.6 \mu\text{m}$ IR laser, $P/a=0.01 \text{ W}\mu\text{m}^{-1}$ and $\tau=30 \text{ s}$. The change in surface height of sub-micron grating features after Shen et al.^[15] is shown in (C).

4.2 Surface smoothing and polishing of glass surfaces

The use of $10.6 \mu\text{m}$ CO_2 lasers to smooth heavily scratched silica surfaces was studied by Nowak et al.,^[16] also providing the first application of capillary flow models to explain the size dependent polishing effects in this application. A more complete description of laser smoothing was published by Shen et al.^[15] who used CFD modeling and calibrated temperature measurements to quantify surface relaxation. **Figure 3 A-B** shows the result of laser polishing on a roughened fused silica sample compared with surface height relaxation function (Fig. 3C) after Shen et al. The roughened surface in Fig. 3 was created by evaporating and recondensing silica using high laser powers ($P/a > 0.025 \text{ W}\mu\text{m}^{-1}$). A roughly 10x reduction in surface roughness was achieved for laser-induced surface temperatures of $\sim 1900 \text{ K}$ over 10's of seconds. By using photolithographic etched gratings and measuring surface height changes as a function of temperature,^[15] surface relaxation was shown to be dominated by capillarity, even at the lowest temperatures studied ($T \sim T_g$). Figure 3C shows the simulated laser smoothing curve $\Delta h(t)/h_0$ vs $1/N_c$ compared with measured height data, where $1/N_c = \sigma\tau/\eta W$ is the inverse capillary number, σ is the surface energy ($\sim 0.3 \text{ N/m}$), η is

viscosity ($\sim 10^7$ Pa.s) and W the feature (e.g. grating pitch) size. Using rastered 1 mm diameter laser beams with dwell times of ~ 30 s, surface roughness of initially 0.5 μm RMS fused silica surfaces could be reduced below 1 nm.

4.3 Heat-affected zone and effect of laser wavelength

Surface polishing and defect annealing of features much smaller than the thermal diffusion length $L_{th} \sim 2\sqrt{D\tau}$ can be considered near isothermal. However, for deep (>100 μm) sub-surface damage caused by mechanical or laser damage, characterization of the thickness of material that can be treated with a given laser system becomes important. Micro-Raman measurements of thermally-induced bonding rearrangement can provide us with a means to characterize this thickness.

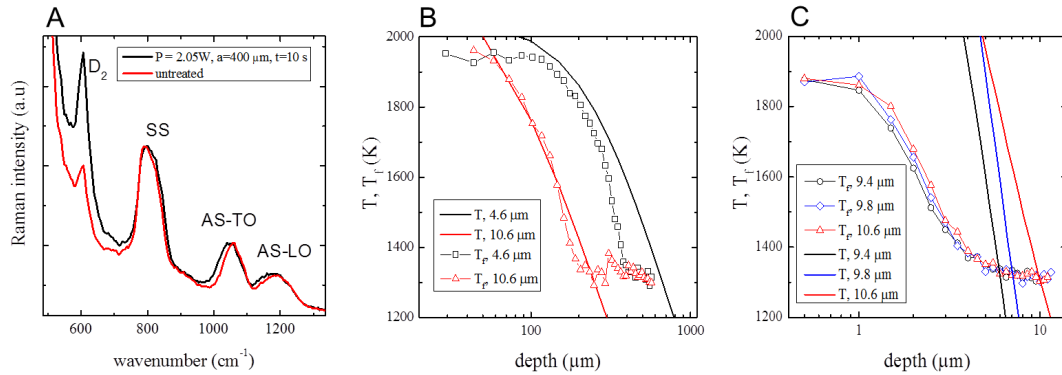


Figure 4: (A) Raman spectrum of pristine and laser annealed fused silica over the range $550 - 1300\text{ cm}^{-1}$ as measured using a confocal microscope. (B) Fictive temperature (T_f) profiles measured along $r=0$ as a function of depth in fused silica for 4.6 μm (\square) and 10.6 μm (Δ) irradiated sites. (C) T_f profiles measured along $r=0$ as a function of depth in fused silica for 9.4 μm (\circ), 9.8 μm (\diamond) and 10.6 μm (Δ) irradiated sites. The pulse length τ for (B) was 300 s with P/a values chosen to limit surface temperatures to $<2000\text{ K}$ while for (C) $t=20\text{ }\mu\text{s}$. Lines are the calculated thermodynamic temperature profiles just prior to laser turn-off.

Figure 4A displays a portion of the measured silica Raman spectrum for both untreated and laser treated silica. Four vibrational modes in Fig. 4A can be identified: D_2 defect at $\sim 600\text{ cm}^{-1}$, a symmetric stretch (SS) mode at $\sim 800\text{ cm}^{-1}$, an asymmetric stretch transverse optic (AS-TO) mode at $\sim 1060\text{ cm}^{-1}$, and an asymmetric stretch longitudinal optic (AS-LO) mode at

$\sim 1200 \text{ cm}^{-1}$. Intensity and frequency changes due to thermal treatment have been described previously.^[6, 7] In particular, the AS-TO mode frequency scales linearly with fictive temperature T_f as $\omega_{TO}(\text{cm}^{-1}) = 1082 - 17 \times 10^{-3} T_f(^{\circ}\text{C})$ and is used to assess T_f in our studies. Figure 4B presents the results of fictive temperature measurements collected along $r=0$, $T_f(z)$, on samples exposed to $\tau=300 \text{ s}$ of 4.6 and 10.6 μm laser heating. The 4.6 μm laser irradiated sites were created with $P=6 \text{ W}$, $a=300 \mu\text{m}$, while for the 10.6 μm laser, $P=5.8 \text{ W}$, $a=340 \mu\text{m}$. These laser parameters were chosen to yield similar ($\sim 2000 \text{ K}$) peak surface temperatures and to minimize material loss due to evaporation. The extent of the heat affected regions, where T_f is elevated above T_g , is greater for the 4.6 μm case ($\sim 400 \mu\text{m}$) versus the 10.6 μm case ($\sim 200 \mu\text{m}$), reflecting the relatively deeper penetration of the light intensity for the former. In addition, it should be noted that the relative axial gradient in $T_f(z)$ is less under 4.6 μm laser heating, which in turn yields smaller density gradients and more limited residual stress. Thus, for annealing of deep sub-surface fracture, mid-IR laser wavelengths with much long absorption depths are more suitable.

On the other hand, minimizing the heat affected zone while maximizing surface heating can be achieved by (1) heating over times less than τ_{th} and (2) tuning the laser wavelength to the maximum of β . As shown below, these laser parameters are more suitable for micro-shaping through material removal. Figure 4C displays the $r=0$, $T_f(z)$ profiles for fused silica exposed to $\tau=12.5 \mu\text{s}$, $P/a \sim 1.1 \text{ W}\mu\text{m}^{-1}$ pulses of $\lambda_L=9.4, 9.8$ and $10.6 \mu\text{m}$ wavelengths. Because $\tau \ll \tau_{th}$, the heat affected region is limited to $\sim 5 \mu\text{m}$ and decreases further as approaches $\lambda_L(\beta_{max}) \sim 9.2 \mu\text{m}$. Though not shown, measured temperatures using our in situ ICCD yielded peak temperatures near $\sim 4000 \text{ K}$ for these pulses, in agreement with predicted temperatures in Sect. 3.

4.3 Sub-surface damage repair using IR lasers

Finally we present examples of wavelength-tuned damage repair using both annealing ($\tau \gg \tau_{th}$, $\beta \ll \beta_{max}$, $T < T_{evap}$) and micro-shaping ($\tau \ll \tau_{th}$, $\beta \sim \beta_{max}$, $T > T_{evap}$) approaches. **Figure 5A-D** are microscope images of a damaged track produced using a several pulses from a UV laser (~ 5 mJ, 3 ns, 351 nm) when viewed from the side. The damage created is

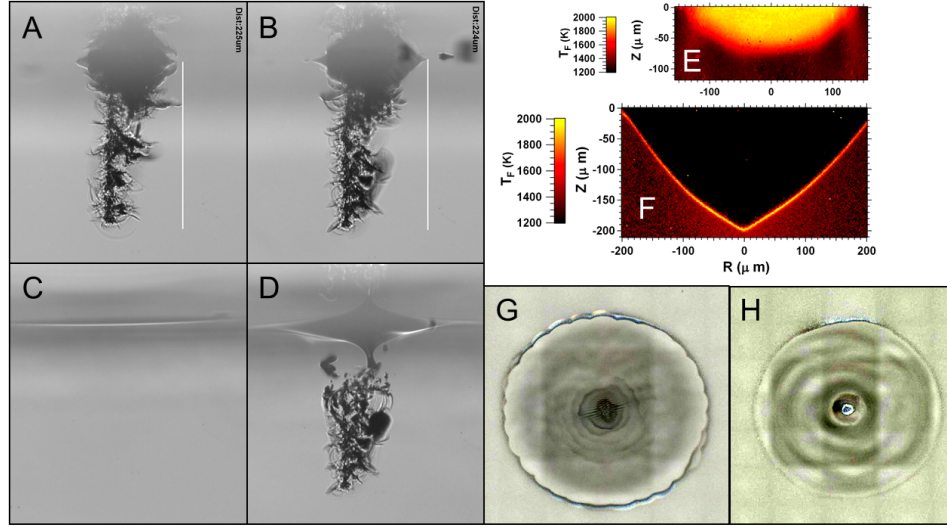


Figure 5: Side views of damage tracks before (A, B) and after annealing with a 4.6 μm (C) and 10.6 μm (D) lasers. The damage track extends 225 μm below surface as indicated by the white bar. Crack healing extended to only 40 μm below surface for the 10.6 μm case, while for the 4.6 μm laser, the cracks are entirely erased.

characterized by a surface crater with a central crack core that extends 225 μm into the bulk, fine hair-line cracks are seen to extend laterally from the central damage core. This damage track was subsequently subjected to 4.6 (Figs. 5A→C) and 10.6 (Figs. 5B→D) μm laser heating with $a=280$ μm and $a=353$ μm respectively. To minimize formation of bubbles, laser power was gradually increased as described previously.^[17] At the end of 300 s irradiation, the original damage track was completely healed, leaving a smooth densified crater that is 3.6 μm deep and 340 μm in diameter at the surface (see Fig. 5C). This healing time is consistent with the predictive $T \sim 1700$ K at the bottom-most crack in Fig. 5A and a predicted crack closure time of $\tau_c \sim \eta W / \pi \sigma$, assuming a crack length W in the range 0.1 to 1 μm.^[8] In contrast,

even after 300 seconds of heating with 10.6 μm laser light at 4.8 W, maximum crack healing extended to only 40 μm below surface as shown in Fig. 5D, in accord with expectation as discussed in the previous sections. Figures 5E-F show side-view fictive temperature maps comparing the use of the non-evaporative approach (E) and the evaporative, micro-shaping approach (F) both at $\lambda_L=10.6 \mu\text{m}$. In Fig. 5F, material has been evaporated away by scanning the beam to produce a conical-shaped micro-pit. As discussed above, a significant difference in heat affected zones can be observed. **Figs. 6G-H** show top view micrographs of micro-cones produced using a laser wavelength near $\beta\sim\beta_{\text{max}}$ (G, $\lambda_L=9.4 \mu\text{m}$) and another far from resonance (H, $\lambda_L=10.9 \mu\text{m}$). As shown, both wavelengths can be used to effectively micro-machine away material, but the more tightly confined heat affected zone for the 9.4 μm case allow less collateral heating as shown above in the T_f analysis.

5. Conclusions

We have described the use of mid- and far-IR laser systems to polish, anneal and micro-shape fused silica surfaces and discussed the effect of laser parameters on material heating. Depending on the polish and surface figure requirements, the IR laser parameters (λ_L , τ , P/a) can be adjusted to optimize the thermal response accordingly. Predicted temperatures based on finite element modelling are found to compare well with experiment. The results shown here have relevance beyond the practical application of damage mitigation in high energy pulsed laser systems to any which require laser-smoothing and shaping of glass surfaces.

[1] W. W. Duley, Academic, New York 1976; N. B. Dahotre, *Lasers in surface engineering*, ASM International, Materials Park, OH 1998.

[2] I. L. Bass, G. M. Guss, M. J. Nostrand, P. J. Wegner, "An Improved Method of Mitigating Laser Induced Surface Damage Growth in Fused Silica Using a Rastered, Pulsed CO₂ Laser", presented at *Laser-Induced Damage in Optical Materials: 2010*, Boulder, CO, USA, 2010.

- [3] F. Y. Genin, A. Salleo, T. V. Pistor, L. L. Chase, Journal of the Optical Society of America a-Optics Image Science and Vision **2001**, 18, 2607.
- [4] S. T. Yang, M. J. Matthews, S. Elhadj, V. G. Draggoo, S. E. Bisson, Journal of Applied Physics **2009**, 106, 1031061.
- [5] S. Elhadj, M. J. Matthews, S. T. Yang, Critical Reviews in Solid State and Materials Sciences **2014**, 39, 175.
- [6] M. J. Matthews, R. M. Vignes, D. Cooke, S. T. Yang, J. S. Stolken, Optics Letters **2010**, 35, 1311.
- [7] A. E. Geissberger, F. L. Galeener, Physical Review B **1983**, 28, 3266.
- [8] S. T. Yang, M. J. Matthews, S. Elhadj, D. Cooke, G. M. Guss, V. G. Draggoo, P. J. Wegner, Appl. Opt. **2010**, 49, 2606.
- [9] A. D. McLachlan, F. P. Meyer, Applied Optics **1987**, 26, 1728.
- [10] R. M. Vignes, T. F. Soules, J. S. Stolken, R. R. Settgast, S. Elhadj, M. J. Matthews, Journal of the American Ceramic Society **2013**, 96, 137.
- [11] S. Elhadj, M. J. Matthews, S. T. Yang, D. J. Cooke, Optics Express **2012**, 20, 1575.
- [12] M. Lax, Journal of Applied Physics **1977**, 48, 3919.
- [13] M. v. Allmen, A. Blatter, *Laser-Beam Interactions with Materials*, Springer, Berlin 1995.
- [14] R. Kitamura, L. Pilon, M. Jonasz, Applied Optics **2007**, 46, 8118.
- [15] N. Shen, M. J. Matthews, J. E. Fair, J. A. Britten, H. T. Nguyen, D. Cooke, S. Elhadj, S. T. Yang, Appl. Surf. Sci. **2010**, 256, 4031.
- [16] K. M. Nowak, H. J. Baker, D. R. Hall, Applied Optics **2006**, 45, 162.
- [17] G. Guss, I. Bass, V. Draggoo, R. Hackel, S. Payne, M. Lancaster, P. Mak, Proc. SPIE - Int. Soc. Opt. Eng. **2006**, 6403, 64030M.